mater.scichina.com link.springer.com

Published online 5 March 2024 | https://doi.org/10.1007/s40843-023-2708-4
Sci China Mater 2024, 67(4): 1160–1172

SPECIAL TOPIC: Computation-assisted Materials Screening and Design

A new 2D Janus family with multiple properties: auxetic behavior, strain-tunable photocatalyst, high Curie temperature ferromagnets, and piezoelectric quantum anomalous Hall insulator

Yu Liu, ShuaiYu Wang and Fengyu Li[*]

ABSTRACT Discovering new two-dimensional (2D) materials, exploring their unique properties and potentials in various applications are of paramount importance to condensed matter physics and materials science. Here based on the diverse properties of the novel square lattice *S*-XS_2 materials found in experiments and computations, we identified 7 novel 2D Janus *S*-XSSe (X = Si, Sn, V, Cr, Mo, Re, Os) monolayers by means of density functional theory computations. Remarkably, both *S*-SiSSe and *S*-SnSSe monolayers possess the auxetic behavior. In addition, they can act as potential photocatalysts, and their photocatalytic performance can be enhanced by changing the pH and applying biaxial strains. Without spin-orbit coupling (SOC), the *S*-VSSe, *S*-CrSSe, and *S*-MoSSe are ferromagnetic half-metals, and have high Curie temperatures T_C (210, 810, and 390 K, respectively). When SOC is included, the *S*-VSSe becomes a quantum anomalous Hall insulator with a sizable gap (45.4 meV) and one chiral edge state (Chern number $C = -1$). By symmetry analysis of semiconducting *S*-XSSe (X = Si, Sn, V) monolayers, only out-of-plane piezoelectric response can be induced by a uniaxial strain in the basal plane, and among them, *S*-VSSe has both the largest out-of-plane piezoelectric coefficients d_{31} and d_{32}, with values of −0.013 and 0.025 pm V^{-1}, respectively. The concurrence of ferromagnetism, topology, and piezoelectricity empowers the *S*-VSSe monolayer as a potential platform for multi-functional spintronics applications with a large gap and high T_C. This theoretical work brings new members, also manifoldness in the properties and functions to the renown 2D materials family.

Keywords: two-dimensional Janus structure, square transition metal dichalcogenides, negative Poisson's ratio, quantum anomalous Hall effect, photocatalyst, piezoelectricity, density functional theory

INTRODUCTION

In 2004, Novoselov *et al.* [1] successfully exfoliated graphene, which can be widely used in the fields of sensors, transistors, new energy batteries and biomaterials due to its outstanding mechanical, electronic, thermal and optical properties [2–4]. Since then, the research on two-dimensional (2D) materials has entered an era of rapid development, which consequently accelerates the emergence of other 2D materials, such as boron nitride (BN) [5], silicene [6], and transition metal dichalcogenide (TMDC) monolayers MX_2 (M = Mo, W; X = S, Se, Te) [7,8]. Among them, TMDCs are one family of the representative 2D materials, which have been widely studied in recent years [9–11], due to the elements contained in the TMDCs are abundant in the earth, with about 3% of sulfur element, which is higher than C, N, B, and P [12]. More importantly, the multiple combinations of transition metal and chalcogen elements make the crystal structures of TMDCs diverse and exhibit rich physical properties [13–15], enabling TMDCs valuable in applications of field effect transistors, photodetectors, nanoelectronics, nanophotonics, and other optoelectronic devices [16–18].

Subsequently, researchers proposed a Janus structure to further investigate its physical properties by replacing one side of the S in the TMDC materials with Se, and MoSSe monolayer was successfully synthesized experimentally after theoretically proving its stability [19]. The internal perpendicular electric field brought about by the broken mirror symmetry brings new quantum effects, such as considering giant spin-orbit coupling (SOC) originating from the d orbitals of the transition metal atoms induces the larger spin splitting from ~150 to ~500 meV [20,21]; surprisingly, Liu *et al.* [22] discovered the intrinsic spin valley-coupled Dirac semimetal (svc-DSM) in Janus BrBiAsCl monolayer; in addition, monolayers Janus XMnY (X, Y = S, Se, Te) are antiferromagnetic and spin-split gapped systems [23]; moreover, polar MXY (M = Mo, W; X, Y = S, Se, Te) monolayers can show additional Rashba spin splitting [24,25]. On the other hand, hydrogen as a clean and sustainable energy source, produced by photocatalytic water-splitting technology, offers the prospect of solving the increasingly serious energy and environmental issues. Ma *et al.* [26] demonstrated that the Janus MoSSe monolayer is potentially an efficient wide solar-spectrum water-splitting photocatalyst due to the optical absorption efficiency and high carrier mobilities. In recent years, seeking 2D multifunctional piezoelectric materials is a compelling problem of novel physics and materials science [27]. Using density functional theory (DFT) computations [28], the strong in-plane piezoelectricity was predicted in MoS_2 monolayer and was later confirmed by experiments [29,30]. Surprisingly, Dong *et al.* [31] reported a strong out-of-plane piezoelectric polarization in the Janus MXY (M = Mo, W; X/Y = S, Se, Te) monolayers due to the lack of reflection symmetry (d_{33} = 5.7–13.5 pm V^{-1} in multilayer

School of Physical Science and Technology, Inner Mongolia University, Hohhot 010021, China
[*] Corresponding author (email: fengyuli@imu.edu.cn)

MXY depending on the stacking pattern), larger than that of the commonly used 3D piezoelectric material AlN (d_{33} = 5.6 pm V^{-1}) [32]. Further, the coexistence of intrinsic piezoelectricity and ferromagnetism, namely piezoelectric ferromagnetism (PFM), was predicted in vanadium dichalcogenides [33]; the combination of piezoelectricity and a topological insulating phase was also achieved in Janus monolayer $SrAlGaSe_4$ [34]; Guo *et al.* [35] successfully predicted an intriguing piezoelectric quantum anomalous hall insulator (PQAHI) Janus Fe_2IX (X = Cl, Br) monolayer, indicating the enormous potential of utilizing the piezoelectric effect to control the quantum or spin transport process, which may lead to novel device applications or scientific breakthroughs.

Numerous previous studies have shown that Janus materials possess a wealth of physical properties and a wide range of application scenarios. However, most of the current studies are focused among the materials with hexagonal lattice. In the experiment, Huang *et al.* [36] successfully prepared square lattice GeS_2 monolayers with *P*-4*m*2 symmetry. In our previous work, a series of *S*-XS_2 (X = Si, Ge, Sn, Pb, Ti, V, Cr, Mn, Zr, Mo, Re, and Os) monolayers with square lattice have been predicted to expand the family of 2D materials. These materials possess excellent properties such as auxetic behavior, high carrier mobility, great electrocatalytic and photocatalytic water-splitting properties, and high Curie temperature [37].

In this work, inspired by the already synthesized Janus monolayer MoSSe, it is possible to achieve the Janus structure based on the *S*-XS_2 monolayer, named *S*-XSSe, and further explore its physical properties. By examining the thermodynamical, dynamical, mechanical, and thermal stabilities *via* first-principles calculations, 7 *S*-XSSe (Si, Sn, V, Cr, Mo, Re, and Os) structures were verified to be stable. Among them, nonmagnetic *S*-SiSSe and *S*-SnSSe semiconductors possess auxetic behavior, and are potential photocatalytic candidates, and their photocatalytic performance can be further enhanced by changing the pH and applying biaxial strains; nonmagnetic *S*-ReSSe and *S*-OsSSe monolayers exhibit metallicity; while ferromagnetic *S*-VSSe, *S*-CrSSe, and *S*-MoSSe are half-metallic, and the Curie temperatures are estimated to be about 210, 810, and 390 K, respectively. By DFT+SOC calculations, the nontrivial topological state of the monolayer *S*-VSSe is firmly confirmed by a nonzero Chern number ($C = -1$) and chiral edge state, and the nontrivial band gap is 45.4 meV. By symmetry analysis, only an out-of-plane piezoelectric response can be induced by a uniaxial strain, and the predicted out-of-plane d_{31} and d_{32} of semiconductor *S*-VSSe is comparable to some 2D known materials, indicating the enormous potential of Janus *S*-VSSe monolayer in developing 2D piezoelectric spin topological devices.

CALCULATION METHODS

The geometric, magnetic, and electronic properties of all the *S*-XSSe monolayers were calculated by projector augmented wave (PAW) projection [38] in Vienna *ab initio* simulation package (VASP) [39]. The Perdew-Burke-Ernzerhof (PBE) functional within the generalized gradient approximation (GGA) approximation was used to describe the exchange and correlation functional [40]. To better describe the strongly correlated d electrons of transition atoms, the GGA+*U* method was employed [41]. The plane-wave cutoff energy was set to 500 eV. The total energy convergence criterion was set at 10^{-5} eV. All the lattice constants and atomic coordinates were optimized with the force on each atom being less than 0.01 eV $Å^{-1}$. A vacuum space larger than 15 Å was used to avoid the interaction between two adjacent slabs. The Γ-centered Monkhorst-Pack *k*-point mesh of 11 × 11 × 1 was adopted in calculations involving structural relaxation calculations, while a denser *k*-point mesh of 21 × 21 × 1 was chosen in the magnetic calculations.

To assess the stability of the *S*-XSSe monolayers, various computational methods were employed. The dynamical stability was evaluated through phonon dispersion calculations using the Phonopy code, which is based on density functional perturbation theory (DFPT) implemented in VASP [42]. The thermal stability was investigated by first-principles molecular dynamics (FPMD) simulations with the PAW method and the PBE functional. In the FPMD simulations, an initial configuration of the *S*-XSSe system, consisting of a 6 × 6 × 1 supercell with 108 atoms, was heated at room temperature (300 K). Each FPMD simulation in an NVT canonical ensemble was performed for a duration of 5 ps with a time step of 1 fs.

The hybrid functional (HSE06) [43] was used to better predict the band structures. Because of the intrinsic dipole in the *S*-XSSe monolayers, a dipole correction in *z* direction was included throughout the calculations of work function [44]. The magnetic anisotropy energy (MAE) was evaluated by a difference in the obtained total energies for two different magnetization directions when considering SOC [45], i.e., MAE = E_x (or E_y) − E_z, the selection of E_x or E_y was determined by the lower energy. The Curie temperature simulations were carried out in the Vampire [46]. The elastic stiffness tensor C_{ij} was calculated by using the strain-stress relationship (SSR) with GGA, and the piezoelectric stress tensor e_{ij} of *S*-SiSSe and *S*-SnSSe (*S*-VSSe) was calculated by the DFPT method [47] using GGA (GGA+SOC). The topological properties were identified by calculating Berry curvature and Chern number *via* Wannier90 [48] and WannierTools [49] packages.

RESULTS AND DISCUSSION

Geometric structures of the *S*-XSSe monolayers

Based on previous work, we discovered 12 stable *S*-XS_2 (X = Si, Ge, Sn, Pb, Ti, V, Cr, Mn, Zr, Mo, Re, and Os) monolayers with square lattice [37]. In this work, we replaced a layer of S by Se to construct the Janus structures and further explored their physical properties. As shown in Fig. 1, the atomistic configuration of 2D *S*-XSSe monolayers is one transition metal atom or main group atom layer sandwiched by S and Se layers. In comparison with the *P*-4*m*2 (no. 115) space group of the *S*-XS_2, the space group of the Janus monolayer *S*-XSSe is reduced to the orthorhombic *Pmm*2 (no. 25), since the different radius of S and Se. To distinguish the hexagonal phases, here we still denote our Janus structure as *S*-XSSe.

To locate the ground state of magnetic order in these 12 *S*-XSSe monolayers, the GGA+*U* method (U_{eff} = 3 eV for transition metal atoms Ti, Cr, Mn, Zr, Mo, Re, and Os [50–53], and U_{eff} = 4 eV for V atom [54], for details see Fig. S1 in Supplementary information) was applied, and four different magnetic configurations, ferromagnetic (FM) and three antiferromagnetic states (AFM1, AFM2, and AFM3) were considered (see Fig. S2). Our calculations revealed that the *S*-VSSe, *S*-CrSSe, and *S*-MoSSe monolayers are FM, *S*-MnSSe monolayer is AFM1, while the other 8 *S*-XSSe (X = Si, Ge, Sn, Pb, Ti, Zr, Re, and Os) monolayers show nonmagnetic behavior (Table S1).

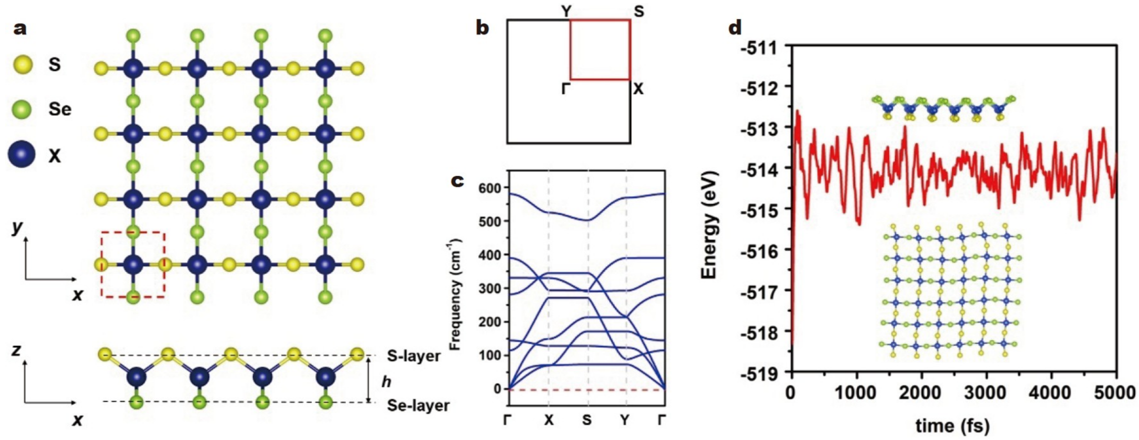

Figure 1 (a) Top and side views of the 4 × 4 × 1 supercell of *S*-XSSe monolayer (the primitive cell is marked by the red rectangle dash line, the yellow, green, and blue balls represent S, Se, and X atoms, respectively); (b) the first Brillouin zone (BZ) of *S*-XSSe monolayers with high symmetric *k* points; (c) the phonon dispersion of *S*-SiSSe; (d) the final structure and energy fluctuation of *S*-SiSSe through a 5 ps FPMD simulation at 300 K.

Table S2 presents the main geometric parameters of 12 *S*-XSSe monolayers in their ground states after structural relaxation, including the lattice constants (*a* and *b*), monolayer thickness (*h*), bond lengths ($r_{\text{X-S/Se}}$), and bond angles ($\theta_{\text{S/Se-X-S/Se}}$). Generally, the lattice constants, monolayer thickness, and bond lengths of these *S*-XSSe monolayers are well correlated with the radius of X. For example, the *a*/*b*, *h*, and $r_{\text{X-S/Se}}$ values increase from 3.43/3.55, 2.82, and 2.18/2.31 Å for Si to 3.97/4.10, 3.32, and 2.55/2.67 Å for Pb, respectively. In addition, since the atomic radius of S is smaller than that of Se, the $r_{\text{X-S}}/a$ is smaller than $r_{\text{X-Se}}/b$.

Stability of *S*-XSSe monolayers

After structural optimization, we got 12 possible stable *S*-XSSe (X = Si, Ge, Sn, Pb, Ti, V, Cr, Mn, Zr, Mo, Re, and Os) structures. To confirm the manufacturability in the experiment, we examined its thermodynamical, dynamical, mechanical, and thermal stabilities.

Firstly, we calculated the cohesive energy (E_{coh}) of *S*-XSSe structures to evaluate their thermodynamical stability, which is defined as

$$E_{\text{coh}} = (E_{\text{X}} + E_{\text{S}} + E_{\text{Se}} - E_{\text{tot}})/3, \quad (1)$$

where E_{tot} is the total energy of the monolayer, and $E_{\text{X}}/E_{\text{S}}/E_{\text{Se}}$ is the energy of an isolated X/S/Se atom. The calculated cohesive energies are shown in Table S2. All the 12 *S*-XSSe monolayers have positive cohesive energies (2.92–5.18 eV atom^{-1}), indicating that thermodynamical stability is satisfied. In addition, these E_{coh} of our *S*-XSSe materials are slightly lower than our previous *S*-XS_2 materials, but comparable to a number of Janus structures of the hexagonal lattice (see Table S2), including MoSSe and WSSe (4.87 and 5.48 eV atom^{-1}, respectively), which have been synthesized experimentally [55], VSSe and CrSSe (4.69 and 3.83 eV atom^{-1}, respectively), which are global minimum structures obtained by CALYPSO [56,57], and SnSSe (3.12 eV atom^{-1}) predicted by theory [58]. Considering that GeS_2 in square lattice has been synthesized experimentally [36], we believe that the Janus structures in this work are expected to be synthesized experimentally in the future [59].

Secondly, the dynamical stability of the *S*-XSSe monolayers was investigated by calculating the phonon dispersions. As shown in Fig. S3, except for AFM *S*-MnSSe, whose imaginary frequencies in its phonon spectrum exceeding −100 cm^{-1}, the other 11 monolayers are dynamically stable as demonstrated by the absence of imaginary frequencies using *S*-SiSSe in Fig. 1c as a reference). Compared with the *S*-XS_2 system, the maximum frequency of phonon dispersion is reduced by less than 50 cm^{-1} (ranging from 300 cm^{-1} of *S*-PbSSe to 580 cm^{-1} of *S*-SiSSe); however, it is comparable to or larger than the maxima of vibrational modes of the hexagonal MoS_2 monolayer (473 cm^{-1}) [60] and black phosphorene (440 cm^{-1}) [61], which suggests that the chemical bonds in the *S*-XSSe structures are still strong.

Then, the mechanical stability of 11 structures (in Table S2) was examined by means of the Born criterion ($C_{11}C_{22} - C_{12}^2 > 0$ and $C_{66} > 0$), and 9 *S*-XSSe (X = Si, Sn, Ti, V, Cr, Zr, Mo, Re, and Os) monolayers show mechanical stability [62]. The mechanical properties are described in detail in the next section.

Finally, the thermal stability of the screened 9 *S*-XSSe monolayers was evaluated by FPMD simulations at 300 K for 5 ps. In Figs S4a and S5, *S*-TiSSe and *S*-ZrSSe were excluded due to their structural distortion, while the total energy fluctuation amplitude of other 7 *S*-XSSe (X = Si, Sn, V, Cr, Mo, Re, and Os) monolayers is less than 4 eV, and these structures were well preserved, indicating that these 7 *S*-XSSe monolayers were thermally stable (using *S*-SiSSe in Fig. 1d as a reference). Considering that the experimental synthesis is at a higher temperature, we raised the temperature of the FPMD simulation to 500 K. The results show that all the structures except *S*-VSSe and *S*-ReSSe can remain thermally stable within 5 ps (see Fig. S4b), implying a high synthesis possibility in the experiments.

To better understand the high stability of 7 stable *S*-XSSe monolayers, we have explored the bonding properties using electron localization functions (ELFs) and Bader charge analysis. Generally, ELF values of 1.0 and 0.5 represent the fully localization and the free electron gas, respectively, while ELF values close to 0 represent areas of low electron density. As displayed in Fig. S6, the *S*-SiSSe shows the covalent bonding because a large number of electrons are accumulated between S/Se and Si atom. For the other 6 *S*-XSSe monolayers, the electrons are accumulated around the S/Se elements, exhibiting ionic bonding characteristics. To qualitatively describe the electron transfer in these structures, we conducted the Bader charge analysis (Table 1) and found that each X atom donates 0.45–2.03 electrons to the

Table 1 Bader charge analysis of *S*-XSSe monolayers (in |*e*|)

	Bader-X	Bader-S	Bader-Se
S-SiSSe	+2.03	−1.13	−0.90
S-SnSSe	+1.27	−0.71	−0.56
S-VSSe	+1.33	−0.73	−0.60
S-CrSSe	+1.00	−0.56	−0.43
S-MoSSe	+1.03	−0.58	−0.45
S-ReSSe	+0.77	−0.47	−0.30
S-OsSSe	+0.45	−0.31	−0.14

adjacent chalcogen atoms. Among them, the Si atom in *S*-SiSSe transfers the highest amount of electrons, as expected from covalent bonding. In addition, S atoms accept more electrons than Se do, due to the larger electronegativity.

Mechanical properties

Based on the 7 stable *S*-XSSe (X = Si, Sn, V, Cr, Mo, Re, and Os) monolayers, we explored the mechanical properties (Table S3). The mechanical properties associated with elastic constants (C_{11}, C_{12}, C_{22}, and C_{66}) can be described by two independent parameters, the orientation-dependent Young's modulus $Y(\theta)$ and Poisson's ratio $v(\theta)$, which can be expressed as follows [63]:

$$Y(\theta) = \frac{C_{11}C_{22} - C_{12}^2}{C_{11}\sin^4\theta + A\sin^2\theta\cos^2\theta + C_{22}\cos^4\theta}, \quad (2)$$

$$v(\theta) = \frac{C_{12}\sin^4\theta - B\sin^2\theta\cos^2\theta + C_{12}\cos^4\theta}{C_{11}\sin^4\theta + A\sin^2\theta\cos^2\theta + C_{22}\cos^4\theta}, \quad (3)$$

where $A = \left(C_{11}C_{22} - C_{12}^2\right)/C_{66} - 2C_{12}$, $B = C_{11} + C_{12} - (C_{11}C_{22} - C_{12}^2)/C_{66}$.

According to the above equations, the Y and v with the variation of angle θ were plotted in Figs S7 and S8, respectively (using *S*-SiSSe in Fig. 2 as a reference). We found that the in-plane Young's modulus of these 7 *S*-XSSe monolayers are all small (less than 100 N m^{-1}) and anisotropic. For *S*-SiSSe and *S*-SnSSe monolayers, the largest value of Young's modulus is along x-direction (95.64 and 54.43 N m^{-1}, respectively), while in y-direction, the Young's modulus is slightly lower (77.42 and 43.07 N m^{-1}, respectively) due to weaker bonding of X–Se than X–S. When X is a transition metal element, all the Young's modulus along x/y-direction are less than 50 N m^{-1} (28.54/27.16, 34.20/29.66, 31.34/22.22, 45.12/12.10, and 25.63/22.83 for *S*-VSSe, *S*-CrSSe, *S*-MoSSe, *S*-ReSSe, and *S*-OsSSe, respectively). The Y values of 7 *S*-XSSe monolayers are much lower than that of hexagonal MoS_2 monolayer (120 N m^{-1}) [64], indicating their promising application as flexible devices.

The Poisson's ratios of the *S*-XSSe monolayers are shown in Fig. S8, ranging from −0.06 to 0.56. Specifically, for *S*-ReSSe, the highest Poisson's ratio is along the x-direction, but other structures have their highest Poisson's ratios along with $\theta = 45° \times n$ (n = 1, 2, 3, 4) directions. Remarkably, the two main group based *S*-XSSe (*S*-SiSSe and *S*-SnSSe) monolayers possess negative Poisson's ratios (NPRs) up to −0.06, which is suggested that interesting auxetic effects have been found, such as resistance to denting [65], high fracture toughness [66], and outstanding vibration or sound absorption capabilities [67]. Besides, the NPR values of both *S*-SiSSe and *S*-SnSSe are more negative than those of δ-phosphorene (−0.027) [68] and borophene (−0.022) [69], which suggests that these two *S*-XSSe monolayers exhibit a more pronounced response as auxetic materials. In order to examine the NPR characteristics of *S*-SiSSe and *S*-SnSSe, we applied uniaxial strain (δ) ranging from −5% to 5% along the x-direction. As shown in Fig. S9, as the uniaxial strain δ_x varies from −5% to 5%, the response in the y-direction (δ_y) increases monotonically (−0.28%–0.34% for *S*-SiSSe, and −0.30%–0.26% for *S*-SnSSe), conforming the NPRs.

To further understand the emerging NPR phenomenon, we examined both geometric and electronic responses exemplified for monolayers *S*-SnSSe and *S*-OsSSe under x-axial strains. The geometric response along the y-direction is related to the bond length l of X–Se and the bond angle θ of Se–X–Se in *S*-XSSe. Therefore, we believe that the NPR and positive Poisson's ratio (PPR) features of the material are mainly related to the above two key parameters in the geometric evolution. Applying uniaxial strains, the changes in θ and l will determine the NPR or PPR characteristics of the material, as shown in Fig. 3a, an increase in θ or l produces NPR and vice versa for PPR feature. In particular, for the two Janus monolayers, under the uniaxial strains ranging from −5% to 5% along the x-direction, the changes in their θ and l, were illustrated in Fig. 3b, c, respectively. As expected, for the NPR material *S*-SnSSe, the changes in θ and l are positively correlated with strain, while the PPR

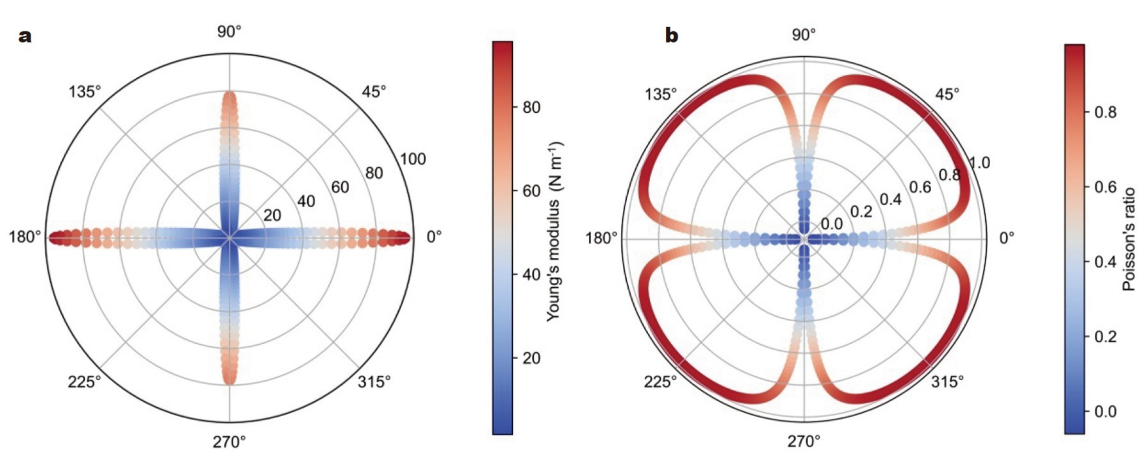

Figure 2 (a) Orientation-dependent in-plane Young's modulus $Y(\theta)$ and (b) Poisson's ratio $v(\theta)$ for the *S*-SiSSe monolayer.

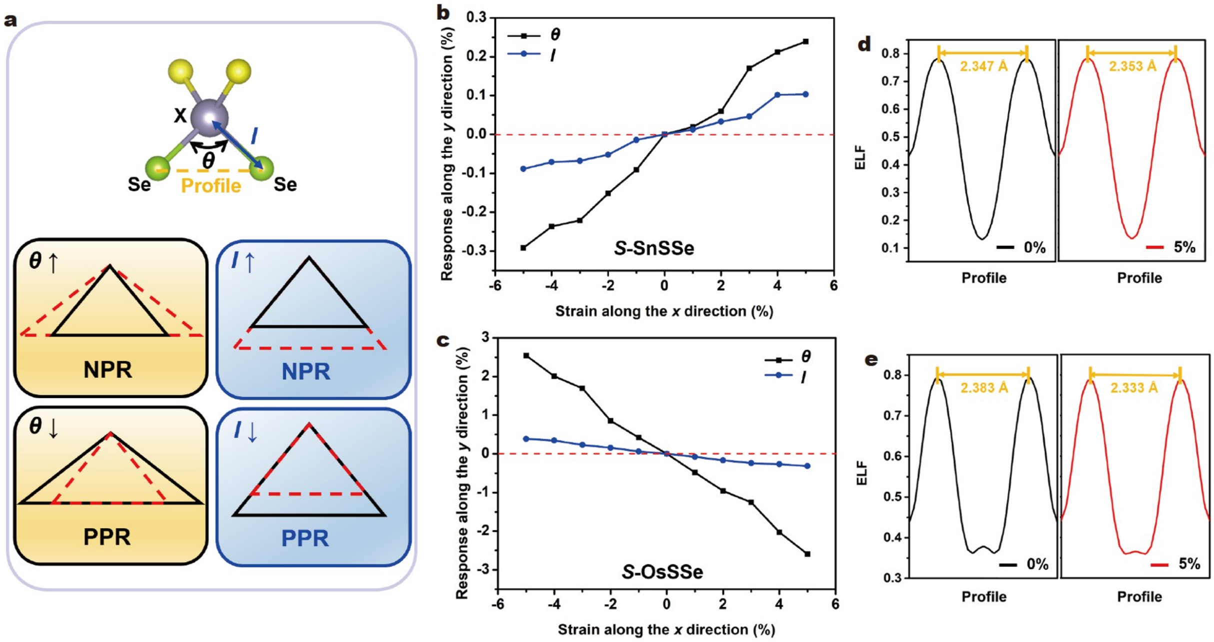

Figure 3 (a) Schematic representation of the bond length l and the bond angle θ in relation to NPR and PPR. Geometric response of (b) *S*-SnSSe and (c) *S*-OsSSe monolayers under the uniaxial (ranging from −5% to 5%) strain along the x-direction. The ELF profile of (d) *S*-SnSSe and (e) *S*-OsSSe under strain along the orange dashed line in (a).

material *S*-OsSSe shows a negative correlation. For some specific materials, the changes in θ and l may be opposite, thus creating competition to decide whether the material is an NPR material or not [70]. This intralayer interaction response originates from the arrangement of electron clouds, which can be visually reflected in the ELF as shown in Fig. 3d, e. When strain was applied from 0% to 5%, the distance of the electron cloud of two Se atoms in *S*-SnSSe was elongated (from 2.347 to 2.353 Å) due to repulsion, while the distance in *S*-OsSSe is shortened (from 2.383 to 2.333 Å).

Electronic properties

To investigate the potential application of *S*-XSSe (X = Si, Sn, V, Cr, Mo, Re, and Os) monolayers, the electronic properties should be investigated. As shown in Fig. 4, we calculated the atom-projected band structures of 7 *S*-XSSe monolayers, and the band structure information (including band gap, band edge position, and band type) of semiconductors is summarized in Table 2. Since the PBE functional usually underestimate the band gap, we used the HSE06 method to have more reliable value of band gap (E_{gap}). The Janus structures have a slight effect on the electronic properties of the original counterparts (see Table S4). The HSE06 results revealed that the *S*-SiSSe and *S*-SnSSe (Fig. 4a, b) are semiconductors with the indirect band gaps of 1.65 and 1.69 eV, respectively, which are significantly reduced compared with the original *S*-SiS_2 and *S*-SnS_2 (2.77 and 2.59 eV, respectively) [37]. The main reason is the difference in atomic radius and electronegativity between S and Se atoms, which will result in inequivalent X–S/Se bond lengths and charge distributions (see the Bader charges in Table 1). For the Janus *S*-SiSSe/*S*-SnSSe monolayer, the larger amount of charges transferred from Si/Sn to S than that to Se atoms. This asymmetry atomic configuration breaks the charge balance along the vertical direction of the monolayers, which leads to a vertical potential alone the out-of-plane direction, and further affects the band structures. From the atom-projected band structures, it can be seen that the valence band maximum (VBM) and conduction band minimum (CBM) are dominantly contributed by p orbital of Se atom and p orbital of Si/Sn atoms. The hybridization of the orbitals moves both CBM and VBM closer to the Fermi level, producing the narrowed band gaps. This trend is also similar to the Janus MXY (M = Ti, Zr, Hf, V, Nb, Ta, Cr, Mo, W; X/Y = S, Se, Te) monolayers of hexagonal lattice [71].

Furthermore, the *S*-ReSSe and *S*-OsSSe (Fig. 4c, d) are metals. The metallicity stems mainly from the d orbitals of the transition metal Re and Os atoms. Remarkably, the ferromagnetic *S*-VSSe, *S*-CrSSe, and *S*-MoSSe monolayers (Fig. 4e–j) exhibit half-metallic characteristics, where the spin-up channel behaves as a metal, and the spin-down channel acts as an indirect band-gap semiconductor (band gap of 2.70, 3.07 and 2.24 eV, respectively), leading to 100% spin polarization in certain spin channel [72].

Photocatalytic properties

It is well known that photocatalysts must be semiconductors, and their band gaps and edge positions must meet certain requirements [73,74]. According to the investigation of electronic properties, the band gaps of *S*-SiSSe and *S*-SnSSe (indirect band gap of 1.65 and 1.69 eV, respectively) monolayers fulfill the first requirement (1.23–3.00 eV) for water splitting. Further, the indirect band gap could efficiently restrain the combination of photoexcited carriers [75]. For the second requirement to photocatalyze water splitting, the band edges must straddle the redox potential of water. The standard reduction potential of H^+/H_2 ($E^{red}(H^+/H_2)$) and the oxidation potential of H_2O/O_2 ($E^{ox}(H_2O/O_2)$) with the inclusion of environmental pH could be expressed by $E^{red}(H^+/H_2) = -4.44 + pH \times 0.059$ eV and $E^{ox}(H_2O/O_2) = -5.67 + pH \times 0.059$ eV, respectively. To obtain the energies of CBM and VBM, the work functions were calculated by $\varphi = E_{vac} - E_F$, where E_{vac} is the energy of a stationary electron

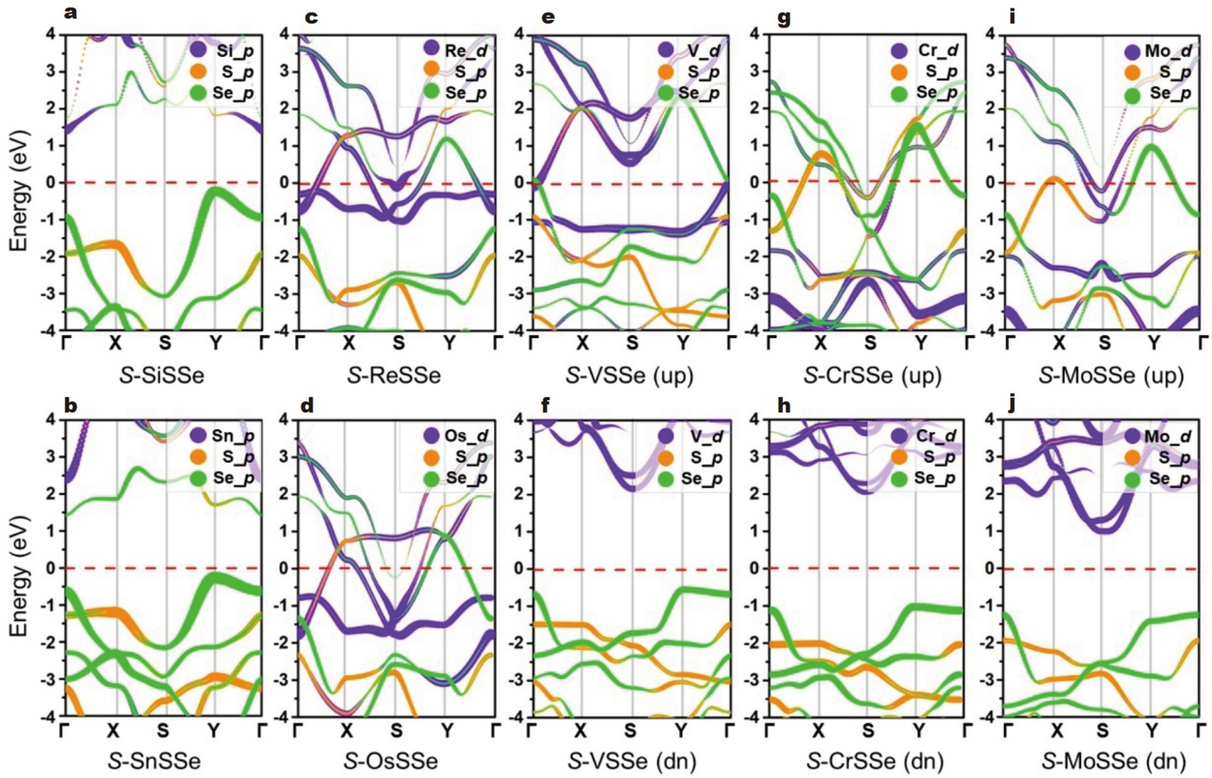

Figure 4 The atom projected band structures of *S*-XSSe monolayers calculated by HSE06 functional. (a) *S*-SiSSe; (b) *S*-SnSSe; (c) *S*-ReSSe; (d) *S*-OsSSe; (e) *S*-VSSe (spin-up); (f) *S*-VSSe (spin-down); (g) *S*-CrSSe (spin-up); (h) *S*-CrSSe (spin-down); (i) *S*-MoSSe (spin-up); (j) *S*-MoSSe (spin-down).

Table 2 The band gaps (E_{gap}, in eV), positions of VBM and CBM, and band type of *S*-XSSe monolayers computed by the HSE06 functional

	S-SiSSe	*S*-SnSSe	*S*-VSSe^{dn}	*S*-CrSSe^{dn}	*S*-MoSSe^{dn}
E_{gap}	1.65	1.69	2.70	3.07	2.24
VBM	Y	Y	Y	Y	Γ
CBM	Γ	Γ	S	S	S-Y
Type	Indirect	Indirect	Indirect	Indirect	Indirect

in the vacuum nearby the surface, E_F is the Fermi energy. Thus, we can take φ as the energy of VBM (E_{VBM}), and the energy of CBM can be obtained *via* the expression of $E_{CBM} = E_{VBM} + E_{gap}$, where E_{gap} is the HSE06 bandgap.

Interestingly, for the *S*-SiSSe and *S*-SnSSe monolayers, due to the electronegativity difference between the S and Se elements, the built-in electric field (E_{eff}) is generated in the direction perpendicular to the plane, resulting in the electrostatic potential difference (ΔΦ), which can promote the separation of electrons and holes [76]. As shown in Fig. 5a, b, the electrostatic potential difference between Se surface and S surface is 0.31 and 0.38 eV for *S*-SiSSe and *S*-SnSSe, respectively. Considering the influence of pH values, as shown in Fig. S10a, b, we found that *S*-SiSSe is suitable as a photocatalyst in alkaline (pH 14) conditions, *S*-SnSSe in acidic or neutral (pH 0 or pH 7) conditions. However, there is a significant energy difference ($\Delta E_1/\Delta E_2$) between the CBM/VBM and the reduction/oxidation potential. For intrinsic *S*-SiSSe and *S*-SnSSe, considering the most appropriate pH, the $\Delta E_1/\Delta E_2$ values are 0.51/0.22 at pH 14 and 0.44/0.40 eV at pH 1 (in Fig. 5c, d), respectively. Thus only *S*-SnSSe possess comparable driving forces for the oxidation and reduction reactions, and have the potential to be an effective photocatalyst for water splitting.

The optical absorption properties of the photocatalyst play a vital role in the entire water-splitting process, and an efficient photocatalyst should be able to absorb visible and ultraviolet (UV) light. Thus, we further investigated the absorption spectra of the *S*-SiSSe and *S*-SnSSe monolayers in *x*, *y*, and *z* directions using the complex dielectric constants (*ε*) at a given frequency with the HSE06 functional [77]. As illustrated in Fig. 5e, f, because of the symmetry of the lattice structure [78], the optical absorption intensity is significantly weaker under *z* than under *x* and *y* directions. Specifically, *S*-SiSSe has a high light absorption efficiency of 10^6 cm^{-1} orders of magnitude in the UV light region, while *S*-SnSSe exhibits a good light absorption efficiency both in the visible and UV regions of the order of 10^5 and 10^6 cm^{-1}, respectively. The high absorption coefficients in both visible and UV light indicate that the *S*-SnSSe monolayer possesses efficient light harvesting capabilities, making the favorable candidates for photocatalyze water splitting. Although *S*-SiSSe possesses a high light absorption efficiency only in the UV region, its reaction driven force is poor compared with *S*-SnSSe. We believe that it can be modulated to increase its light absorption efficiency, e.g., by strain engineering [26,79].

Strain engineering is an effective way to tune the band gap, which in turn affects the position of the band edges. In order to explore how strain affects the photocatalytic properties, we applied the biaxial strains of −6%–6% (with an interval of 2%), and calculated their band gaps and band edge positions by HSE06 method (see Fig. S11 and Fig. 6a, b). Generally, the CBM and VBM positions of *S*-XSSe (X = Si, Sn) decrease with

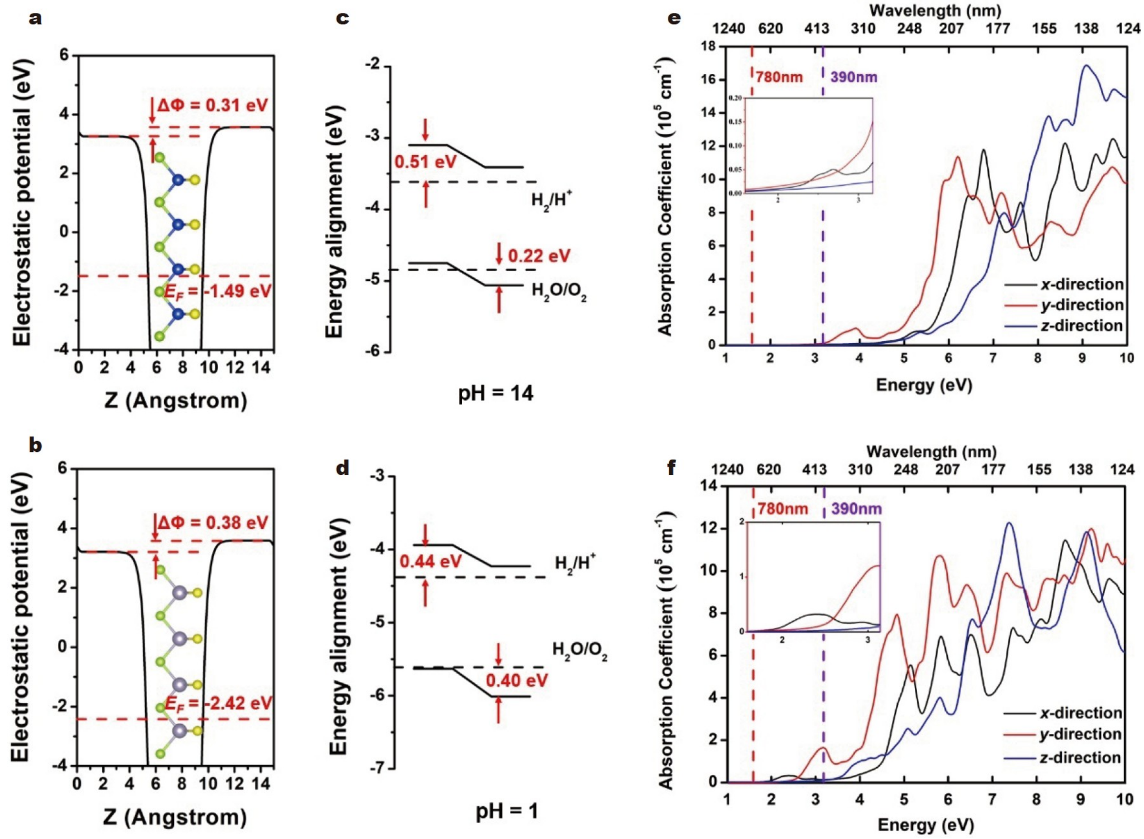

Figure 5 The surface potential differences of (a) *S*-SiSSe and (b) *S*-SnSSe monolayer. The alignment of energy levels for monolayer (c) *S*-SiSSe at pH 14 and (d) *S*-SnSSe at pH 1 with regard to the water redox potentials. The dashed lines indicate the reduction and oxidation potentials of water. Optical absorption spectra for monolayers for (e) *S*-SiSSe and (f) *S*-SnSSe in *x*, *y*, and *z* directions using the HSE06 method.

increasing tensile strain. In acidic environment (pH 0), only *S*-SiSSe at 6% tensile strain, *S*-SnSSe at −2%–4% strain, their band edge positions simultaneously cross the redox potential of water, can be used as a photocatalysts; while in alkaline (pH 14) condition, the band edge positions of *S*-SiSSe and *S*-SnSSe cross the redox potential of water under strains of 0%–4% and −6%–−4%, respectively. Therefore, the reaction driving force of both *S*-XSSe (X = Si, Sn) can be tuned by applying biaxial strain as well as varying the acidic-alkaline conditions (pH from 0 to 14, we only considered two extreme conditions). Furthermore, the absorption of *S*-SiSSe and *S*-SnSSe extends progressively to the lower energy part with increasing the biaxial strains. When the strain reaches 6%, the light absorption peaks of *S*-SiSSe (in Fig. 6c–e) in the *x*, *y* directions reach the visible region and the light absorption coefficients reach 10^4 and 10^5 cm^{-1}, respectively, and the absorption in the *z* direction is a little weaker and almost reaches 10^4 cm^{-1} in the visible light region; for *S*-SnSSe (in Fig. 6f–h), the absorption coefficients reach 10^4 cm^{-1} in the *x* direction and 10^5 cm^{-1} in the *y* direction in both tension and compression, and the absorption peaks are in the visible region, while in the *z* direction the light absorption peaks are close to the visible region only at 6% tensile strain and the absorption coefficients reach 10^5 cm^{-1}. The overall performances are superior to that of the famous 2D g-C_3N_4 photocatalyst [80], demonstrating that our *S*-SiSSe and *S*-SnSSe are potentially efficient photocatalytic materials.

Moreover, for *S*-SiSSe and *S*-SnSSe monolayers, the hydrogen evolution reaction (HER) and oxygen evolution reaction (OER) during water splitting were simulated using the model developed by Nørskov [81]. We used a supercell of 5 × 5 × 1 for HER and OER calculations (eight adsorption sites on each surface were considered: S1–S8, see Fig. S12), and ultimately we found that HER and OER are most likely to occur at the S5 site of the S-surface. The Gibbs free energies of these electrochemical elementary steps in the OER were calculated at zero cell potential (U = 0) and the equilibrium potential (U = 1.23 V), respectively, see Fig. S13. For the OER, the rate-determining step (RDS) is the oxidation of *O to *OOH with a limiting reaction barrier (ΔG_{max}) of 2.17 and 0.52 eV at U = 1.23 eV (3.40 and 1.75 eV at U = 0 eV) for *S*-SiSSe and *S*-SnSSe, respectively. The results are slightly higher or much better than 1.92 eV of 2H-MoS_2 at U = 1.23 eV [82]. Meanwhile the ΔG_{max} of HER are 1.17 and 1.82 eV for *S*-SiSSe and *S*-SnSSe, respectively, both lower than 2.1 eV of 2H-MoS_2 toward HER [83]. Therefore, both *S*-SiSSe and *S*-SnSSe, especially the latter one, have more potential as photocatalysts for OER.

Carrier mobility

The high mobility of photogenerated carriers is important to reduce the carrier recombination rate, thus ensuring better photocatalytic performance. The deformation potential (DP) theory was employed to calculate the carrier mobility *via* the following equation [84]:

$$\mu = \frac{e\hbar^3 C_{2D}}{k_B T m^* m_d^* E_l^2}. \tag{4}$$

The detail for calculations can be found in the Supplementary information. The value of elastic modulus C_{2D}, DP constant E_l

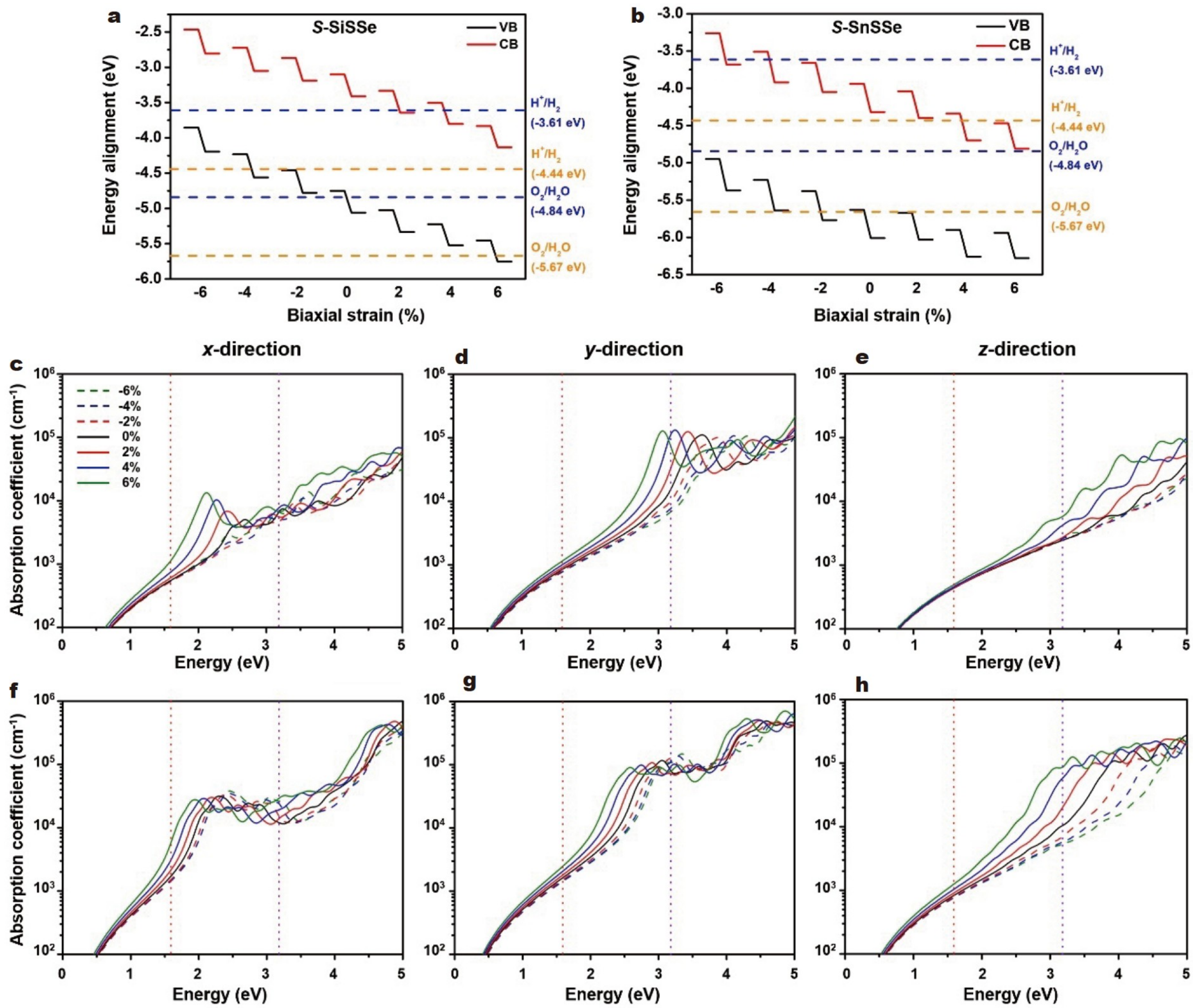

Figure 6 The band edge positions of (a) *S*-SiSSe and (b) *S*-SnSSe under biaxial strains. The orange and blue dashed lines represent the redox potentials under acidic (pH 0) and alkaline (pH 14) conditions, respectively. Biaxial strain dependent optical absorption coefficient of *S*-SiSSe in (c) *x*, (d) *y* and (e) *z* directions, respectively. Biaxial strain dependent optical absorption coefficient of *S*-SnSSe in (f) *x*, (g) *y* and (h) *z* directions, respectively. The visible zone is indicated between the red and purple dotted lines.

(Fig. S14), effective mass m^*, and carrier mobility μ are listed in Table 3. In the *x*-direction, the electron and hole mobility for *S*-SiSSe/*S*-SnSSe are 575.93/166.73 and 66.91/36.97 $cm^2\ V^{-1}\ s^{-1}$; in *y*-direction, they are 2512.81/130.12 and 152.61/39.29 $cm^2\ V^{-1}\ s^{-1}$. These values are comparable or higher than that of the 2D Janus WSSe (125.01/723.42 and 124.70/433.22 $cm^2\ V^{-1}\ s^{-1}$ for electron and hole mobility along the armchair/zigzag direction, respectively) [79]. Generally, larger electron and hole mobility discrepancy could induce a lower bulk and surface recombination of photoexcited carriers during the migration, thus increasing the photocatalytic efficiency. Along the *x* (*y*) direction, the electron mobility is about 9/3 (16/3) times higher than the hole mobility of SiSSe/SnSSe. Thus, due to the large carrier mobility discrepancy, both *S*-SiSSe and *S*-SnSSe monolayers have the capability to strengthen the separation of photogenerated carriers, then can serve as excellent photocatalysts.

Magnetic properties

The MAE is an important requirement for the thermal stability of magnetic orderings, which is the key factor for the long-range ferromagnetic orderings of 2D materials. MAE also indicates the energy required to overcome the barrier when switching the direction of the magnetic moment from the easy axis to the hard axis [85]. For the 3 FM *S*-XSSe (X = V, Cr, and Mo) monolayers, the MAE values are 0.379 meV/V, −0.166 meV/Cr, and 1.646 meV/Mo, respectively (see Table 4), indicating that the easy axis for both *S*-VSSe and *S*-MoSSe are along the out-of-plane direction, while for *S*-CrSSe is in-plane direction.

Then we evaluated the Curie temperature (T_C) of these 3 monolayers by Monte Carlo simulations based on the Heisenberg model. The Hamiltonian is described by [86]

$$H = -J_1\sum_{\langle i,j\rangle} S_iS_j - J_2\sum_{\langle i,k\rangle} S_iS_k - J_3\sum_{\langle i,l\rangle} S_iS_l - AS_i^{Z}S_i^{Z}, \quad (5)$$

where the J_1, J_2, and J_3 are the nearest (N), next-nearest (NN), and next-next-nearest (NNN) magnetic exchange interaction parameters (as shown in Fig. S2), S_i is the spin vector of each atom, A is the anisotropy energy parameter, which can be obtained by using the MAEs as A = MAE/$|S|^2$, and S_i^{Z} is the Z

Table 3 Computed effective mass (m^*) of the electron and hole, elastic constant (C_{2D}), DP constant (E_l), and carrier mobilities (μ) for the *S*-SiSSe and *S*-SnSSe monolayers

	Type	m^*/m_0		C_{2D} (N m^{-1})		E_l (eV)		μ (cm^2 V^{-1} s^{-1})	
		m_x^*	m_y^*	C_{2D}-x	C_{2D}-y	E_l-x	E_l-y	μ_x	μ_y
S-SiSSe	Hole	−0.27	−1.35	95.93	77.65	13.70	3.65	66.91	152.61
	Electron	0.31	0.40			8.07	6.12	575.93	2512.81
S-SnSSe	Hole	−0.38	−2.23	54.57	43.18	9.49	3.38	36.97	39.29
	Electron	0.43	0.31			6.67	7.91	166.73	130.12

Table 4 On-site magnetic moments (M) for transition metal, exchange coupling parameters J_1, J_2, and J_3, MAE, and Curie temperature (T_C) of *S*-VSSe, *S*-CrSSe, *S*-MoSSe, and CrI_3 monolayer (italics indicate values in Ref. [87])

	M (μ_B)	J_1 (meV)	J_2 (meV)	J_3 (meV)	MAE (meV)	T_C (K)
S-VSSe	1.00	134.68	110.02	−1.60	0.379	210
S-CrSSe	2.00	137.91	107.25	−2.85	−0.166	810
S-MoSSe	2.00	51.14	70.29	−6.27	1.646	390
CrI_3	3.00	2.76/*2.7*	0.565	−0.149	0.725/*0.803*	57/*45*

component of the spin vector. Four magnetic configurations of FM, AFM1, AFM2, and AFM3 are used to extract the magnetic parameters:

$$H_{(\mathrm{AFM1})} = H_0 - 4J_1S^2 + 4J_2S^2 + 8J_3S^2 - A\,|\,S\,|^2, \quad (6)$$

$$H_{(\mathrm{AFM2})} = H_0 + 4J_1S^2 + 4J_2S^2 - 8J_3S^2 - A\,|\,S\,|^2, \quad (7)$$

$$H_{(\mathrm{AFM3})} = H_0 + 4J_1S^2 - 4J_2S^2 + 8J_3S^2 - A\,|\,S\,|^2, \quad (8)$$

$$H_{(\mathrm{FM})} = H_0 - 4J_1S^2 - 4J_2S^2 - 8J_3S^2 - A\,|\,S\,|^2. \quad (9)$$

As shown in Table 4, we have obtained the value of on-site magnetic moments (M), exchange coupling parameters (J_1, J_2, and J_3) and T_C of *S*-VSSe, *S*-CrSSe, and *S*-MoSSe monolayers, respectively. The T_C of *S*-VSSe, *S*-CrSSe, and *S*-MoSSe are about 210, 810, and 390 K, respectively, as shown in Fig. 7, which can be comparable or higher than a recently studied 2H-VSSe monolayer (346 K) [56]. Our method predicts the T_C for the synthesized CrI_3 monolayer to be 57 K (see Fig. S15). This is in good agreement with the experimental and theoretical values (45 K) [87], which validates the Monte Carlo method used in this work.

Topological properties

From the electronic properties, we give the band structure of FM state *S*-VSSe monolayer by HSE06 method (in Fig. 4e, f), where the gapless Dirac semimetal for spin-up and a large-gap insulator for spin-down (2.70 eV), namely the 2D half Dirac semimetal. In this section, we focus on the electronic structure and topological properties of *S*-VSSe by GGA theory. Fig. 8a, b show the energy band structures of the *S*-VSSe monolayer with GGA and GGA+SOC. When the SOC is absent, the energy band structure is in high agreement with the results of the HSE06 method. It is found that the spin-up bands near the Fermi level are mainly contributed by d_{xy} of V, p_x and p_y of S/Se atoms (see Fig. S16). The special electronic structures suggest that the *S*-VSSe might be a QAH insulator when the SOC is included.

To verify whether the *S*-VSSe is a QAH insulator or not, we reexamined the band structure including SOC, and found that a band gap of 45.4 meV is opened near the Fermi level in the Γ-X path, as shown in Fig. 8b. If the band gap is topologically nontrivial, it suggests that QAH effect can be realized. Then we calculated the Chern number (C) of the *S*-VSSe monolayer by integrating the Berry curvature ($\Omega_z(k)$) of the occupied bands:

$$C = \frac{1}{2\pi}\int_{\mathrm{BZ}} \mathrm{d}^2k\,\Omega_z(k), \quad (10)$$

$$\Omega_z(k) = \nabla_k \times i < \mu_{n,k} \,|\, \nabla_k \mu_{n,k} >, \quad (11)$$

where $\mu_{n,k}$ is the lattice periodic part of the Bloch wave functions. The calculations reveal that nonzero Berry curvatures only distribute along the Γ-X path (see Fig. 4i). The topologically nontrivial Chern number of $C = -1$ was obtained by integrating the Berry curvatures, corresponding to the quantized Hall conductance of $\sigma_{xy} = -e^2/h$, where h is the reduced Planck constant. We also found a chiral edge state along the edge (see Fig. 8c), further confirming the QAH characteristic of *S*-VSSe monolayer.

Piezoelectricity

Considering our semiconductor monolayer *S*-XSSe (X = Si, Sn, and V), it is possible to use them as piezoelectric materials due to the prohibition of current leakage. By symmetry analysis, our *Pmm*2 space group lacks reflectional symmetry across the *xy* plane, but has reflectional symmetry across the *xz* or *yz* plane. This means that in-plane piezoelectricity will disappear, and only out-of-plane piezoelectricity can exist. The third-rank piezoelectric stress tensor e_{ijk} and strain tensor d_{ijk} can be used to describe the piezoelectric effects of a material, which include ionic and electronic contributions. A detailed derivation of the piezoelectric coefficients can be seen in the supplementary material.

After derivation, only vertical piezoelectric polarization (e_{31}/d_{31} and $e_{32}/d_{32} \neq 0$) exists in our *S*-XSSe monolayers. The e_{31}/e_{32} indicates the amount of polarization change in the z direction produced by the monolayer under the influence of an applied strain in the x/y direction in the plane. The unit cell is used to calculate the e_{31}/d_{31} and e_{32}/d_{32} of Janus monolayer *S*-XSSe (X = Si, Sn, and V), and the results are summarized in

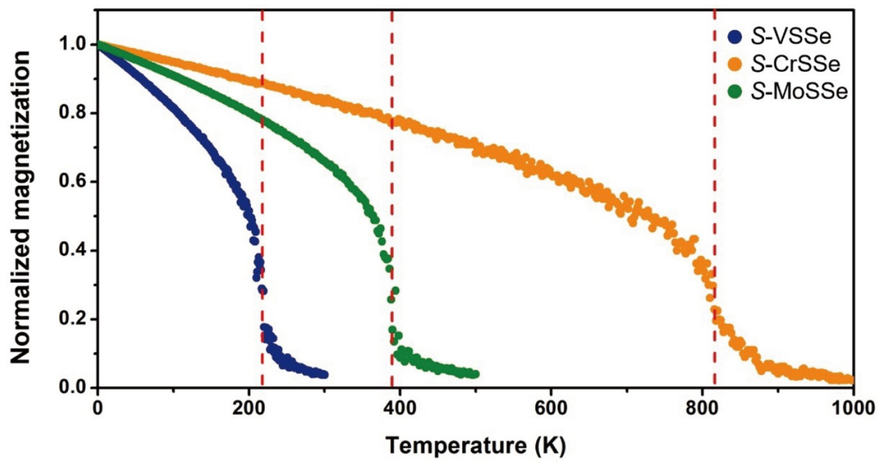

Figure 7 Normalized magnetization of *S*-VSSe, *S*-CrSSe, and *S*-MoSSe monolayers by performing Monte Carlo simulations.

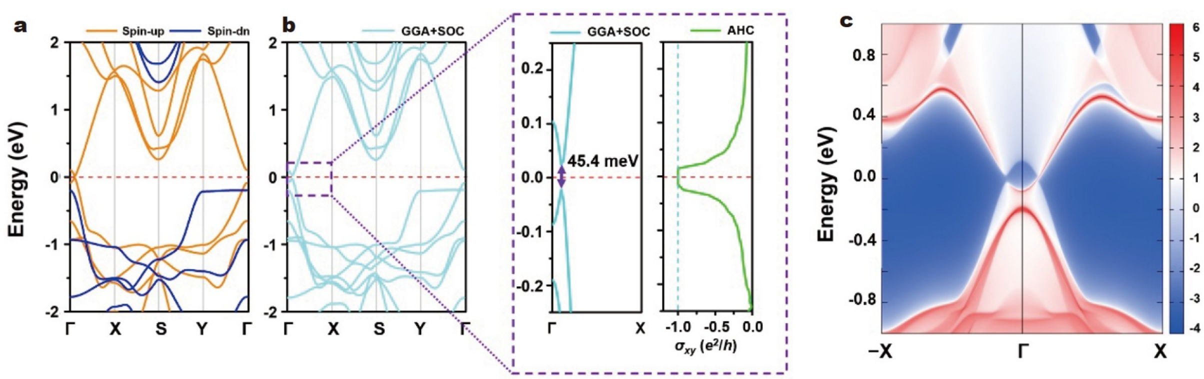

Figure 8 The energy band structure of *S*-VSSe monolayer (a) without and (b) with SOC at the FM ground state. The orange (blue) lines represent the band structure in the spin-up (spin-down). The enlarged image shows the Dirac cone in the GGA+SOC at the ΓX line, opened a gap of 45.4 meV, and the corresponding anomalous Hall conductivity (AHC). (c) The topological edge state of *S*-VSSe monolayer along the (010) direction.

Table 5. The piezoelectric strain coefficient d_{ij} is an important factor in measuring the efficiency of mechanical and electrical energy conversion of piezoelectric devices, and is a bridge between theoretical predictions and practical applications. In our *S*-XSSe systems, the out-of-plane piezoelectric coefficients of *S*-SiSSe and *S*-SnSSe are relatively tiny, with d_{31} and d_{32} less than 0.004 pm V^{-1}, whereas the *S*-VSSe monolayer has both the largest out-of-plane piezoelectric coefficients d_{31} and d_{32} of −0.013 and 0.025 pm V^{-1}, respectively, which are comparable with the values of some 2D materials with out-of-plane piezoelectricity properties reported previously, such as Janus TMD monolayers MoSSe, MoSeTe, and MoSTe (0.020, 0.030, and 0.028 pm V^{-1}, respectively) [31].

CONCLUSIONS

By constructing the Janus structure based on the square disulfide monolayers, we obtain 7 *S*-XSSe (X = Si, Sn, V, Cr, Mo, Re, and Os) monolayers which have good thermodynamical, dynamical, mechanical and thermal stabilities. Among them, *S*-SiSSe and *S*-SnSSe possess auxetic behavior. Through electronic structure calculations, it was found that the *S*-SiSSe and *S*-SnSSe are indirect band-gap semiconductors with HSE06 band gaps of 1.65 and 1.69 eV, respectively. The suitable band-edge positions, efficient absorption coefficients in the visible region, and large carrier mobility differences render them as potential water-splitting photocatalysts. Furthermore, it is found that the pH and external biaxial strains can effectively increase the solar-to-hydrogen energy conversion efficiency. Thus, the findings not only predicted a promising photocatalyst for water splitting under visible light irradiation, but also proposed a method to improve the photocatalytic efficiency and extend the absorption spectrum.

While ferromagnetic *S*-VSSe, *S*-CrSSe, and *S*-MoSSe are half-metallic, the Curie temperatures are estimated to be about 210, 810, and 390 K respectively. By GGA+SOC calculations, the intriguing 2D PQAHI *S*-VSSe is predicted. The nontrivial topological state of the monolayer *S*-VSSe, identified by Chern number $C = -1$ and chiral edge state, has a nontrivial band gap of 45.4 meV. The out-of-plane piezoelectric d_{31} and d_{32} of *S*-VSSe is −0.013 and 0.025 pm V^{-1}, comparable to some 2D known materials, which is highly desirable for ultrathin piezo-

Table 5 Piezoelectric coefficients e_{31}/d_{31} and e_{32}/d_{32} of *S*-XSSe (X = Si, Sn, and V) monolayers

S-XSSe	e_{31} (pC m^{-1})	e_{32} (pC m^{-1})	d_{31} (pm V^{-1})	d_{32} (pm V^{-1})
S-SiSSe	0.272	0.103	0.004	0.002
S-SnSSe	0.154	0.051	0.003	0.001
S-VSSe	0.103	0.696	−0.013	0.025

electric devices. These indicate the enormous potential of Janus *S*-VSSe monolayer in developing 2D piezoelectric spin topological devices. Our predicted close to room temperature PQAHI is of crucial importance to fundamental research and to the future development of electronics, piezoelectronics and spintronics, and these findings provide new opportunities to realize novel practical quantum applications.

It is worth noting that our 7 Janus *S*-XSSe materials are only constructed based on the 12 *S*-XS_2 in our previous theoretical calculations, so it is still worth investigating the stability of the other X elements in our Janus *S*-XSSe system, and there is a possibility that other novel physical properties may be discovered. Our work not only theoretically proposes a series of novel 2D Janus materials, but also provides guidance for further theoretical as well as experimental studies.

Received 25 September 2023; accepted 29 November 2023; published online 5 March 2024

1 Novoselov KS, Geim AK, Morozov SV, *et al.* Electric field effect in atomically thin carbon films. Science, 2004, 306: 666–669
2 Cooper DR, D'Anjou B, Ghattamaneni N, *et al.* Experimental review of graphene. ISRN Condensed Matter Phys, 2012, 2012: 1–56
3 Zhang Y, Tang TT, Girit C, *et al.* Direct observation of a widely tunable bandgap in bilayer graphene. Nature, 2009, 459: 820–823
4 Craciun MF, Russo S, Yamamoto M, *et al.* Tuneable electronic properties in graphene. Nano Today, 2011, 6: 42–60
5 Pacilé D, Meyer JC, Zettl A, *et al.* The two-dimensional phase of boron nitride: Few-atomic-layer sheets and suspended membranes. Appl Phys Lett, 2008, 92: 133107
6 Vogt P, De Padova P, Quaresima C, *et al.* Silicene: Compelling experimental evidence for graphenelike two-dimensional silicon. Phys Rev Lett, 2012, 108: 155501
7 Wang QH, Kalantar-Zadeh K, Kis A, *et al.* Electronics and optoelectronics of two-dimensional transition metal dichalcogenides. Nat Nanotech, 2012, 7: 699–712
8 Kuc A, Zibouche N, Heine T. Influence of quantum confinement on the electronic structure of the transition metal sulfide TS_2. Phys Rev B, 2011, 83: 245213
9 Yuan X, Yang M, Wang L, *et al.* Structural stability and intriguing electronic properties of two-dimensional transition metal dichalcogenide alloys. Phys Chem Chem Phys, 2017, 19: 13846–13854
10 Jariwala D, Sangwan VK, Lauhon LJ, *et al.* Emerging device applications for semiconducting two-dimensional transition metal dichalcogenides. ACS Nano, 2014, 8: 1102–1120
11 Guo H, Lu N, Wang L, *et al.* Tuning electronic and magnetic properties of early transition-metal dichalcogenides *via* tensile strain. J Phys Chem C, 2014, 118: 7242–7249
12 Morgan JW, Anders E. Chemical composition of earth, venus, and mercury. Proc Natl Acad Sci USA, 1980, 77: 6973–6977
13 Zhu CR, Wang G, Liu BL, *et al.* Strain tuning of optical emission energy and polarization in monolayer and bilayer MoS_2. Phys Rev B, 2013, 88: 121301
14 Raiber S, Faria Junior PE, Falter D, *et al.* Ultrafast pseudospin quantum beats in multilayer WSe_2 and $MoSe_2$. Nat Commun, 2022, 13: 4997
15 Ding Y, Wang Y, Ni J, *et al.* First principles study of structural, vibrational and electronic properties of graphene-like MX_2 (M = Mo, Nb, W, Ta; X = S, Se, Te) monolayers. Phys B-Condensed Matter, 2011, 406: 2254–2260
16 Radisavljevic B, Whitwick MB, Kis A. Integrated circuits and logic operations based on single-layer MoS_2. ACS Nano, 2011, 5: 9934–9938
17 Miller CW, Sharoni A, Liu G, *et al.* Quantitative structural analysis of organic thin films: An X-ray diffraction study. Phys Rev B, 2005, 72: 104113
18 Radisavljevic B, Radenovic A, Brivio J, *et al.* Single-layer MoS_2 transistors. Nat Nanotech, 2011, 6: 147–150
19 Zhang J, Jia S, Kholmanov I, *et al.* Janus monolayer transition-metal dichalcogenides. ACS Nano, 2017, 11: 8192–8198
20 Zhu ZY, Cheng YC, Schwingenschlögl U. Giant spin-orbit-induced spin splitting in two-dimensional transition-metal dichalcogenide semiconductors. Phys Rev B, 2011, 84: 153402
21 Zibouche N, Kuc A, Musfeldt J, *et al.* Transition-metal dichalcogenides for spintronic applications. Annalen der Phys, 2014, 526: 395–401
22 Liu Z, Li L, Cui L, *et al.* Intrinsic spin-valley-coupled Dirac state in Janus functionalized β-BiAs monolayer. Nanoscale Horiz, 2021, 6: 283–289
23 Sattar S, Islam MF, Canali CM. Monolayer MnX and Janus XMnY (X, Y = S, Se, Te): A family of two-dimensional antiferromagnetic semiconductors. Phys Rev B, 2022, 106: 085410
24 Bychkov YA, Rashba EI. Oscillatory effects and the magnetic susceptibility of carriers in inversion layers. J Phys C-Solid State Phys, 1984, 17: 6039–6045
25 Cheng YC, Zhu ZY, Tahir M, *et al.* Spin-orbit-induced spin splittings in polar transition metal dichalcogenide monolayers. EPL, 2013, 102: 57001
26 Ma X, Wu X, Wang H, *et al.* A Janus MoSSe monolayer: A potential wide solar-spectrum water-splitting photocatalyst with a low carrier recombination rate. J Mater Chem A, 2018, 6: 2295–2301
27 Lin P, Pan C, Wang ZL. Two-dimensional nanomaterials for novel piezotronics and piezophototronics. Mater Today Nano, 2018, 4: 17–31
28 Duerloo KAN, Ong MT, Reed EJ. Intrinsic piezoelectricity in two-dimensional materials. J Phys Chem Lett, 2012, 3: 2871–2876
29 Wu W, Wang L, Li Y, *et al.* Piezoelectricity of single-atomic-layer MoS_2 for energy conversion and piezotronics. Nature, 2014, 514: 470–474
30 Zhu H, Wang Y, Xiao J, *et al.* Observation of piezoelectricity in free-standing monolayer MoS_2. Nat Nanotech, 2015, 10: 151–155
31 Dong L, Lou J, Shenoy VB. Large in-plane and vertical piezoelectricity in janus transition metal dichalchogenides. ACS Nano, 2017, 11: 8242–8248
32 Almaghbash ZAAR, Arbouche O, Dahani A, *et al.* Significant improvement in the piezoelectric properties and electromechanical coupling factors of wurtzite AlN compound under high pressures. J Comput Electron, 2021, 20: 2420–2430
33 Yang J, Wang A, Zhang S, *et al.* Coexistence of piezoelectricity and magnetism in two-dimensional vanadium dichalcogenides. Phys Chem Chem Phys, 2019, 21: 132–136
34 Guo SD, Zhu YT, Mu WQ, *et al.* A piezoelectric quantum spin Hall insulator with Rashba spin splitting in Janus monolayer $SrAlGaSe_4$. J Mater Chem C, 2021, 9: 7465–7473
35 Guo SD, Mu WQ, Xiao XB, *et al.* Intrinsic room-temperature piezoelectric quantum anomalous hall insulator in Janus monolayer Fe_2IX (X = Cl and Br). Nanoscale, 2021, 13: 12956–12965
36 Huang Y, Pan YH, Yang R, *et al.* Universal mechanical exfoliation of large-area 2D crystals. Nat Commun, 2020, 11: 2453
37 Liu Y, Li W, Li F, *et al.* Computational discovery of diverse functionalities in two-dimensional square disulfide monolayers: auxetic behavior, high curie temperature ferromagnets, electrocatalysts, and photocatalysts. J Mater Chem A, 2023, 11: 20254–20269
38 Kresse G, Joubert D. From ultrasoft pseudopotentials to the projector augmented-wave method. Phys Rev B, 1999, 59: 1758–1775
39 Kresse G, Furthmüller J. Efficient iterative schemes for *ab initio* total-energy calculations using a plane-wave basis set. Phys Rev B, 1996, 54: 11169–11186
40 Perdew JP, Burke K, Ernzerhof M. Generalized gradient approximation made simple. Phys Rev Lett, 1996, 77: 3865–3868
41 Liechtenstein AI, Anisimov VI, Zaanen J. Density-functional theory and strong interactions: Orbital ordering in Mott-Hubbard insulators. Phys Rev B, 1995, 52: R5467–R5470
42 Baroni S, de Gironcoli S, Dal Corso A, *et al.* Phonons and related crystal properties from density-functional perturbation theory. Rev Mod Phys, 2001, 73: 515–562
43 Heyd J, Scuseria GE, Ernzerhof M. Hybrid functionals based on a screened Coulomb potential. J Chem Phys, 2003, 118: 8207–8215
44 Neugebauer J, Scheffler M. Adsorbate-substrate and adsorbate-adsorbate interactions of Na and K adlayers on Al (111). Phys Rev B, 1992, 46: 16067–16080

45 Wang D, Wu R, Freeman AJ. First-principles theory of surface magnetocrystalline anisotropy and the diatomic-pair model. Phys Rev B, 1993, 47: 14932–14947
46 Evans RFL, Fan WJ, Chureemart P, *et al.* Atomistic spin model simulations of magnetic nanomaterials. J Phys-Condens Matter, 2014, 26: 103202
47 Wu X, Vanderbilt D, Hamann DR. Systematic treatment of displacements, strains, and electric fields in density-functional perturbation theory. Phys Rev B, 2005, 72: 035105
48 Mostofi AA, Yates JR, Lee YS, *et al.* Wannier90: A tool for obtaining maximally-localised Wannier functions. Comput Phys Commun, 2008, 178: 685–699
49 Wu QS, Zhang SN, Song HF, *et al.* WannierTools: An open-source software package for novel topological materials. Comput Phys Commun, 2018, 224: 405–416
50 He J, Ding G, Zhong C, *et al.* Cr_2TiC_2-based double MXenes: Novel 2D bipolar antiferromagnetic semiconductor with gate-controllable spin orientation toward antiferromagnetic spintronics. Nanoscale, 2019, 11: 356–364
51 Wang G. Theoretical prediction of the intrinsic half-metallicity in surface-oxygen-passivated Cr_2N MXene. J Phys Chem C, 2016, 120: 18850–18857
52 He J, Lyu P, Nachtigall P. New two-dimensional Mn-based MXenes with room-temperature ferromagnetism and half-metallicity. J Mater Chem C, 2016, 4: 11143–11149
53 Li SS, Hu SJ, Ji WX, *et al.* Emergence of ferrimagnetic half-metallicity in two-dimensional MXene $Mo_3N_2F_2$. Appl Phys Lett, 2017, 111: 202405
54 Zhou B, Wang X, Mi W. Superior electronic structure of two-dimensional 3D transition metal dicarbides for applications in spintronics. J Mater Chem C, 2018, 6: 4290–4299
55 Qin Y, Sayyad M, Montblanch ARP, *et al.* Reaching the excitonic limit in 2D janus monolayers by *in situ* deterministic growth. Adv Mater, 2022, 34: 2106222
56 Zhang C, Nie Y, Sanvito S, *et al.* First-principles prediction of a room-temperature ferromagnetic Janus VSSe monolayer with piezoelectricity, ferroelasticity, and large valley polarization. Nano Lett, 2019, 19: 1366–1370
57 Wu Y, Liu Q, Shi P, *et al.* High temperature ferromagnetic metal: A Janus CrSSe monolayer. Phys Chem Chem Phys, 2023, 25: 9958–9964
58 Zhang W, Zhang J, He C, *et al.* Constructing Janus SnSSe and graphene heterostructures as promising anode materials for Li-ion batteries. Intl J Energy Res, 2022, 46: 267–277
59 Lu AY, Zhu H, Xiao J, *et al.* Janus monolayers of transition metal dichalcogenides. Nat Nanotech, 2017, 12: 744–749
60 Molina-Sánchez A, Wirtz L. Phonons in single-layer and few-layer MoS_2 and WS_2. Phys Rev B, 2011, 84: 155413
61 Qin G, Yan QB, Qin Z, *et al.* Anisotropic intrinsic lattice thermal conductivity of phosphorene from first principles. Phys Chem Chem Phys, 2015, 17: 4854–4858
62 Wang J, Yip S, Phillpot SR, *et al.* Crystal instabilities at finite strain. Phys Rev Lett, 1993, 71: 4182–4185
63 Cadelano E, Colombo L. Effect of hydrogen coverage on the Young's modulus of graphene. Phys Rev B, 2012, 85: 245434
64 Peng Q, De S. Outstanding mechanical properties of monolayer MoS_2 and its application in elastic energy storage. Phys Chem Chem Phys, 2013, 15: 19427–19437
65 Lakes RS, Elms K. Indentability of conventional and negative Poisson's ratio foams. J Composite Mater, 1993, 27: 1193–1202
66 Choi JB, Lakes RS. Fracture toughness of re-entrant foam materials with a negative Poisson's ratio: Experiment and analysis. Int J Fract, 1996, 80: 73–83
67 Evans KE, Alderson A. Auxetic materials: Functional materials and structures from lateral thinking. Adv Mater, 2000, 12: 617–628
68 Jiang JW, Park HS. Negative Poisson's ratio in single-layer black phosphorus. Nat Commun, 2014, 5: 4727
69 Zhong H, Huang K, Yu G, *et al.* Electronic and mechanical properties of few-layer borophene. Phys Rev B, 2018, 98: 054104
70 Yu L, Wang Y, Zheng X, *et al.* Emerging negative Poisson's ratio driven by strong intralayer interaction response in rectangular transition metal chalcogenides. Appl Surf Sci, 2023, 610: 155478
71 Shi W, Wang Z. Mechanical and electronic properties of Janus monolayer transition metal dichalcogenides. J Phys-Condens Matter, 2018, 30: 215301
72 Moulkhalwa H, Zaoui Y, Obodo KO, *et al.* Half-metallic and half-semiconductor gaps in Cr-based chalcogenides: DFT+U calculations. J Supercond Nov Magn, 2019, 32: 635–649
73 Wang L, Liu J, Wang H, *et al.* Forming electron traps deactivates self-assembled crystalline organic nanosheets toward photocatalytic overall water splitting. Sci Bull, 2021, 66: 265–274
74 Wan Y, Wang L, Xu H, *et al.* A simple molecular design strategy for two-dimensional covalent organic framework capable of visible-light-driven water splitting. J Am Chem Soc, 2020, 142: 4508–4516
75 Zhao P, Ma Y, Lv X, *et al.* Two-dimensional III2-VI3 materials: Promising photocatalysts for overall water splitting under infrared light spectrum. Nano Energy, 2018, 51: 533–538
76 Gao X, Shen Y, Liu J, *et al.* Boosting the photon absorption, exciton dissociation, and photocatalytic hydrogen- and oxygen-evolution reactions by built-in electric fields in Janus platinum dichalcogenides. J Mater Chem C, 2021, 9: 15026–15033
77 Saha S, Sinha TP. Electronic structure, chemical bonding, and optical properties of paraelectric $BaTiO_3$. Phys Rev B, 2000, 62: 8828–8834
78 Liu TY, Zhang QR, Zhuang SL. First principle studies on the electronic structures and absorption spectra under polarized light for the $PbWO_4$ crystal with oxygen vacancy. Phys Lett A, 2004, 333: 473–477
79 Ju L, Bie M, Tang X, *et al.* Janus WSSe monolayer: An excellent photocatalyst for overall water splitting. ACS Appl Mater Interfaces, 2020, 12: 29335–29343
80 Ma X, Lv Y, Xu J, *et al.* A strategy of enhancing the photoactivity of g-C_3N_4 *via* doping of nonmetal elements: A first-principles study. J Phys Chem C, 2012, 116: 23485–23493
81 Nørskov JK, Rossmeisl J, Logadottir A, *et al.* Origin of the overpotential for oxygen reduction at a fuel-cell cathode. J Phys Chem B, 2004, 108: 17886–17892
82 German E, Gebauer R. Why are MoS_2 monolayers not a good catalyst for the oxygen evolution reaction? Appl Surf Sci, 2020, 528: 146591
83 Qiao W, Xu W, Xu X, *et al.* Construction of active orbital *via* single-atom cobalt anchoring on the surface of 1T-MoS_2 basal plane toward efficient hydrogen evolution. ACS Appl Energy Mater, 2020, 3: 2315–2322
84 Bardeen J, Shockley W. Deformation potentials and mobilities in non-polar crystals. Phys Rev, 1950, 80: 72–80
85 Jiang S, Nazir S, Yang K. Origin of the large interfacial perpendicular magnetic anisotropy in MgO/Co_2FeAl. Phys Rev B, 2020, 101: 134405
86 Wu Q, Zhang Y, Zhou Q, *et al.* Transition-metal dihydride monolayers: A new family of two-dimensional ferromagnetic materials with intrinsic room-temperature half-metallicity. J Phys Chem Lett, 2018, 9: 4260–4266
87 Webster L, Yan JA. Strain-tunable magnetic anisotropy in monolayer $CrCl_3$, $CrBr_3$, and CrI_3. Phys Rev B, 2018, 98: 144411

Acknowledgements This work was supported by the National Natural Science Foundation of China (11964024 and 12364038), the "Grassland Talents" Project of Inner Mongolia Autonomous Region (12000-12102613), and the Young Science and Technology Talents Cultivation Project of Inner Mongolia University (21200-5223708). The computational support from the PARATEAR at Guangzhou Supercomputer Center was acknowledged.

Author contributions The initial idea was developed by Li F, Liu Y and Wang S performed the calculations under Li F's supervision. All authors participated in the data analysis and writing and reading of the paper. Li F managed the project.

Conflict of interest The authors declare that they have no conflict of interest.

Supplementary information Experimental details and supporting data are available in the online version of the paper.

Yu Liu started his Master's degree at Inner Mongolia University in 2020. After that, he continued his education as a PhD candidate under the supervision of Prof. Fengyu Li. His research focuses on theoretical design and physical property exploration of novel two-dimensional materials based on first-principles calculations.

Fengyu Li received her PhD degree from Dalian University of Technology (2012) and University of Puerto Rico (2014). After spending two years at University of Puerto Rico as a postdoc researcher, she served as a professor at Inner Mongolia University. Her research mainly focuses on low-dimensional materials design and simulation from first-principles and machine learning.

具有多种性质的新型二维Janus家族：拉胀行为、应变可调的光催化剂、高居里温度铁磁体和压电量子反常霍尔绝缘体

刘宇，王帅宇，李锋钰*

摘要 发现新的二维材料并探索其独特性质与潜在应用是凝聚态物理与材料科学的重要课题. 在此，我们基于在实验和计算中报道的具有多种性质的新型方晶格*S*-XS_2二维材料，通过密度泛函理论计算，确定了7种具有近似方晶格的新型二维Janus *S*-XSSe (X = Si, Sn, V, Cr, Mo, Re和Os)单层材料. 值得注意的是，*S*-SiSSe和*S*-SnSSe单层都具有拉胀行为，此外，由于具有合适的带边位置、可见光区的高效吸收系数和较大的载流子迁移率差，它们是潜在的光催化剂，而且光催化性能还可以通过改变 pH值和施加双轴应变来提高. 在不考虑自旋轨道耦合(SOC)时，*S*-VSSe，*S*-CrSSe和S-MoSSe是铁磁半金属，并具有较高的居里温度T_C (分别为210，810和390 K). 加入SOC后，*S*-VSSe成为量子反常霍尔(QAH)绝缘体，具有较大的带隙(45.4 meV)和一个手性边缘态(陈数$C = -1$). 通过对半导体*S*-XSSe (X = Si, Sn, V) 单层的对称性分析，基底面上的单轴应变只能诱发面外压电响应. 其中，*S*-VSSe的面外压电系数d_{31}和d_{32}最大，分别为-0.013和0.025 pm V^{-1}. 压电性、拓扑性和铁磁性的共存使单层*S*-VSSe成为具有大带隙和高T_C的多功能自旋电子学应用的潜在平台. 我们的理论工作将给二维材料增添新家族，并有望带来更广阔的应用.

